The current issue and full text archive of this journal is available at
www.emeraldinsight.com/0961-5539.htm

Entropy generation analysis for the free surface turbulent flow during laser material processing

Dipankar Chatterjee
Department of Mechanical & Mining Machinery Engineering, Indian School of Mines University, Dhanbad, India, and
Suman Chakraborty
Department of Mechanical Engineering, Indian Institute of Technology Kharagpur, Kharagpur, India

Received 28 February 2007
Revised 6 February 2008
Accepted 20 February 2008

Abstract

Purpose – The purpose of this paper is to carry out a systematic energy analysis for predicting the first and second law efficiencies and the entropy generation during a laser surface alloying (LSA) process.
Design/methodology/approach – A three-dimensional transient macroscopic numerical model is developed to describe the turbulent transport phenomena during a typical LSA process and subsequently, the energy analysis is carried out to predict the entropy generation as well as the first and second law efficiencies. A modified k–ε model is used to address turbulent molten metal-pool convection. The phase change aspects are addressed using a modified enthalpy-porosity technique. A kinetic theory approach is adopted for modelling evaporation from the top surface of the molten pool.
Findings – It is found that the heat transfer due to the strong temperature gradient is mainly responsible for the irreversible degradation of energy in the form of entropy production and the flow and mass transfer effects are less important for this type of phase change problem. The first and second law efficiencies are found to increase with effective heat input and remain independent of the powder feed rate. With the scanning speed, the first law efficiency increases whereas the second law efficiency decreases.
Research limitations/implications – The top surface undulations are not taken care of in this model which is a reasonable approximation.
Practical implications – The results obtained will eventually lead to an optimized estimation of laser parameters (such as laser power, scanning speed, etc.), which in turn improves the process control and reduces the cost substantially.
Originality/value – This paper provides essential information for modelling solid–liquid phase transition as well as a systematic analysis for entropy generation prediction.
Keywords Thermodynamic properties, Modelling, Turbulent flow, Heat transfer
Paper type Research paper

Nomenclature

a_P, a_P^0 = Discretization equation coefficients
b = Small number to avoid division by zero
c = Specific heat
C = Species concentration
D = Species mass diffusion coefficient
f_l = Liquid fraction of the solute
g = Acceleration due to gravity
g_i = Chemical potential
h = Convective heat transfer coefficient
H = Total enthalpy
J = Vaporization flux
k = Turbulent kinetic energy
K = Thermal conductivity
k_B = Boltzmann constant
k_p = Partition coefficient
K_m = Morphological constant

International Journal of Numerical Methods for Heat & Fluid Flow
Vol. 19 Nos. 3/4, 2009
pp. 303-328

0961-5539
DOI 10.1108/09615530910938308

L = Latent heat of fusion
L_v = Latent heat of vaporization
m = Mass per atom
m_f = Powder feedrate
$\dot{m}$ = Mass flux
N_s = Entropy generation number
n = Normal direction
P = Pressure
P_S = Partial pressure
Q = Actual power input
r_q = Radius of heat input
R = Universal gas constant
S = Entropy
s = Specific entropy
T = Temperature
T_0 = Initial substrate temperature
t = Time
u = x-component of velocity
u_{scan} = Laser scanning speed
V_S = Evaporating surface velocity
v = y-component of velocity
v_n = Interface velocity
w = z-component of velocity
x,y,z = Co-ordinates fixed to the laser source

Greek variables

β_T = Coefficient of volumetric expansion of heat
β_C = Coefficient of volumetric expansion of solute
η = Laser efficiency
η_I = First second law efficiency
η_{II} = Second law efficiency
μ_t = Eddy viscosity
Γ_{eff} = Effective diffusion coefficient in general transport equation
ΔH = Latent enthalpy
ε = Dissipation rate
ε_r = Emissivity
ϕ = General scalar variable
σ_{sur} = Surface tension
σ_t = Turbulent Prandtl number
σ_c = Turbulent Schmidt number
σ_{rad} = Stefan–Boltzmann constant
ρ = Density
ρ_v = Density of metal vapour
μ = Molecular viscosity
ς = Source term

Superscript

n = Iteration level

Subscripts

k = Phase
l = Liquid region
max = Maximum value
m = Mushy region
n = Normal direction
old = Old iteration value
p = Nodal coefficient
r = Reference
s = Solid region

Introduction

Laser surface alloying (LSA) finds extensive applications in various types of industries, such as automotive, aerospace, power industries, etc. This surface engineering technique offers an excellent scope for tailoring the surface microstructure and/or composition of a component. This involves melting of a pre-deposited layer or concomitantly added alloying elements/compounds with a part of the underlying substrate by the directed energy laser beam to form an alloyed zone confined to a shallow depth within a very short interaction time. From the macroscopic point of

view, the entropy generation and second law efficiency are strongly dependent on the thermal histories in the fusion zone and the nearby-unmelted region. Also, molten metal flow is known to have a considerable effect on these thermal histories and solidification processes. Therefore, in order to predict the second law efficiency of the process accurately, it is very important to have a thorough knowledge of the transport mechanism inside the laser molten pool, which leads to a final resolidified microstructure.

Efficiency analysis of the thermal systems is an important issue to the thermal system designers as the optimal design criteria of such systems depends on the idea of minimizing entropy generation in the systems. During the pulse or continuous beam laser heating process, energy is stored inside the substrate material when the laser beam is impinged on it and it is removed when the beam is removed. The rate of these energy storage and removal processes ultimately governs the morphology of the material. Consequently, the exergy analysis of the laser heating process may become fruitful in optimizing the laser parameters, which in turn improves the process control and reduces the cost substantially. To achieve these goals, a number of researchers worked on the efficiency analysis of thermal systems in the past (Mathiprakasam and Beeson (1984), Krane (1987), Bejan (1982a, b, 1987), Haddad *et al.* (2000), Shuja *et al.* (2002, 2007)). Krane (1985) introduced the concept of entropy generation number. Badar *et al.* (1993) investigated the thermoeconomics of the sensible heat thermal energy system. Bejan (1982a, b) applied the second law analysis to the thermal energy storage system. His approach is based on minimizing the destruction of thermodynamic availability as opposed to maximizing the total amount of thermal energy storage. Yilbas (1999) developed a three-dimensional laser-heating model along with the entropy generation consideration following the electron-kinetic theory approach. However, any mathematical model pertaining to the energy analysis for a coupled turbulent momentum, heat and mass transfer in presence of a dynamically changing interface is yet to be reported in the literature, till date, to the best of the authors' knowledge.

Accordingly, the aim of the present work is to carry out a systematic energy analysis for predicting the first and second law efficiencies and the entropy generation during an LSA process. A modified enthalpy-porosity technique is used to model the dynamic solid–liquid phase transition. A modified k–ε model is used to address the turbulent transport. The source terms of both k and ε equations are so devised that a smooth transition from a completely solid state to a fully liquid state can be achieved by the same set of equations. On validation the model shows good matching with the available experimental results.

Mathematical formulation

Physical description of the problem

The physical problem involves melting of thin layer of a substrate with a continuous beam laser moving with a constant scanning speed u_{scan} in the negative x-direction and simultaneously feeding an alloying element inside the laser generated melt pool (refer to Figure 1). The intense heat from the laser beam creates a large temperature gradient in the substrate which induces a strong surface tension driven flow. As soon as the laser moves resolidification occurs which leads to the final alloyed microstructure. The flow and thermo-solutal histories are essential to predict the microstructural composition and entropy generation in the process.

Governing equations for fluid flow and heat transfer

The general governing transport equation for fluid flow and heat transfer in a convection–diffusion conservative form can be given as:

$$\frac{\partial(\rho\phi)}{\partial t} + \frac{\partial}{\partial x_i}(\rho u_i \phi) = \frac{\partial}{\partial x_i}\left(\Gamma_{eff}\frac{\partial \phi}{\partial x_i}\right) + \varsigma_\phi \tag{1}$$

where ϕ is a vector of conserved quantities, such as mass, momentum or energy, x_i is the coordinate in the Cartesian system, u_i is the component of mean velocity in direction x_i, Γ_{eff} is the effective diffusion coefficient for the variable ϕ and ς_ϕ is the source term for the dependent variable ϕ. Following the Reynolds averaging technique the equivalent single-phase governing equations for the incompressible, Newtonian liquid flow in the melt pool can be constructed in a Cartesian coordinate system fixed with the moving laser source (since it is a moving heat source problem, a moving coordinate system is adopted to formulate the governing equations and consequently, source terms will arise as a result of the coordinate transformation) and the corresponding values of ϕ, Γ_{eff} and ς_ϕ for various conservation equations are given in Table I.

Enthalpy-porosity formulation

In the present formulation, a single domain fixed-grid enthalpy-porosity model (Brent *et al.*, 1988) is used for modelling the phase change process. In this method, the morphology of the phase change domain can be treated as an equivalent porous medium that offers a frictional resistance towards fluid flow in that region. This resistance can be conveniently formulated using Darcy's model in association with the Cozeny–Karman relationship (Brent *et al.*, 1988), which leads to the source term $A\bar{u}_i$ in the momentum equation, where A is given as:

$$A = -K_m\left[\frac{(1-f_l)^2}{f_l^3 + b}\right]\bar{u}_i \tag{2}$$

where, f_l is the liquid fraction given by $\Delta H/L$, with ΔH being the latent enthalpy content of a control volume and L being the latent heat of fusion. The term ΔH can be expressed as:

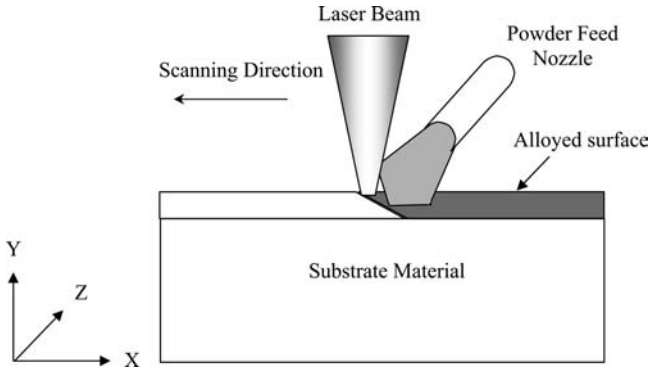

Figure 1.
Schematic diagram of a typical LSA process

$$\begin{aligned}\Delta H = f(T) = L \quad &: \bar{T} > T_l \\ = f_l L \quad &: T_s \le \bar{T} < T_l \\ = 0 \quad &: \bar{T} < T_s \end{aligned} \tag{3}$$

where T_s and T_l are the solidus and liquidus temperatures, respectively.

In Equation (2), K_m is a large number (~10^8) and b is a small number (~10^{-3}) to avoid division by zero. The above formulation effectively ensures that the velocity undergoes a smooth transition from a zero value in the solid region to a finite value in the liquid region.

Modelling of turbulence parameters

Modelling of Reynolds stress term $\left(-\rho\overline{u_i' u_j'}\right)$. In the present analysis, the Reynolds stress term is modelled by assuming a turbulent viscosity of the form:

$$-\rho\overline{u}_i' u_j' = \mu_t\left(\frac{\partial \bar{u}_i}{\partial x_j} + \frac{\partial \bar{u}_j}{\partial x_i}\right) - \frac{2}{3}\delta_{ij}k \tag{4}$$

Governing equations	ϕ	Γ_{eff}	ς_ϕ
Continuity	1	0	0
x-momentum	$\bar{u}$	$\mu + \mu_t$	$\frac{\partial}{\partial x_j}\left(\Gamma_{eff}\frac{\partial \bar{u}}{\partial x_j}\right) - \frac{\partial p}{\partial x} - A\bar{u} - \rho u_{scan}\frac{\partial \bar{u}}{\partial x}$
y-momentum	$\bar{v}$	$\mu + \mu_t$	$\frac{\partial}{\partial x_j}\left(\Gamma_{eff}\frac{\partial \bar{v}}{\partial x_j}\right) - \frac{\partial p}{\partial y} - A\bar{v} - \rho u_{scan}\frac{\partial \bar{v}}{\partial x} + \rho g\left[\beta_T\left(\bar{T} - T_r\right) + \beta_C\left(\bar{C} - C_r\right)\right]$
z-momentum	$\bar{w}$	$\mu + \mu_t$	$\frac{\partial}{\partial x_j}\left(\Gamma_{eff}\frac{\partial \bar{w}}{\partial x_j}\right) - \frac{\partial p}{\partial z} - A\bar{w} - \rho u_{scan}\frac{\partial \bar{w}}{\partial x}$
Energy	$\bar{T}$	$\frac{K}{c} + \frac{\mu_t}{\sigma_t}$	$-\frac{1}{c}\left[\frac{\partial(\rho\Delta H)}{\partial t} + \frac{\partial\left(\rho u_j \Delta H\right)}{\partial x_j}\right] - \rho u_{scan}\frac{\partial \bar{T}}{\partial x}$
Species	$\bar{C}$	$\rho D + \frac{\mu_t}{\sigma_c}$	$-\rho u_{scan}\frac{\partial \bar{C}}{\partial x}$
Turbulent kinetic energy	k	$\mu + \frac{\mu_t}{\sigma_k}$	$\mu_t\left(\frac{\partial \bar{u}_i}{\partial x_j} + \frac{\partial \bar{u}_j}{\partial x_i}\right)\frac{\partial \bar{u}_i}{\partial x_j} - g\beta_T\frac{\mu_t}{\sigma_t}\frac{\partial \bar{T}}{\partial y} - g\beta_C\frac{\mu_t}{\sigma_c}\frac{\partial \bar{C}}{\partial y} - \rho\varepsilon - \rho u_{scan}\frac{\partial k}{\partial x}$
Dissipation rate of turbulent kinetic energy	ε	$\mu + \frac{\mu_t}{\sigma_\varepsilon}$	$\left[\mu_t\left(\frac{\partial \bar{u}_i}{\partial x_j} + \frac{\partial \bar{u}_j}{\partial x_i}\right)\frac{\partial \bar{u}_i}{\partial x_j} - g\beta_T\frac{\mu_t}{\sigma_t}\frac{\partial \bar{T}}{\partial y} - g\beta_C\frac{\mu_t}{\sigma_c}\frac{\partial \bar{C}}{\partial y}\right]\frac{C_{\varepsilon 1}\varepsilon}{k} - \rho\frac{C_{\varepsilon 2}\varepsilon^2}{k} - \rho u_{scan}\frac{\partial \varepsilon}{\partial x}$

Table I.
Table of diffusion coefficients and source terms for various conservation equations

where

$$\mu_t = \sqrt{f_l} C_\mu \frac{\rho k^2}{\varepsilon} \tag{5}$$

In Equation (5), C_μ is a constant, whose value has been determined from shear-flow experiments (Komatsu and Matsunaga, 1986). It is reported that C_μ varies from 0.08 to 0.09 (Chen and Law, 1998). For the present study C_μ is taken to be 0.09. It is important to note that in a standard high Reynolds number $k - \varepsilon$ model, the term $\sqrt{f_l}$ does not appear. In the present problem, the whole domain is not composed of a single phase so the formulation should ensure a reduction of eddy viscosity, thermal conductivity and mass diffusivity so that the effective diffusivity approaches to their respective molecular values along the solid–liquid interface, and merge with single-phase turbulent flow conditions in the fully liquid region. It can be seen from Equation (5) the eddy viscosity goes to zero in the solid phase as liquid fraction is identically zero in solid and in liquid phase the eddy viscosity assumes the standard expression for single-phase flow problems as $\sqrt{f_l}$ is identically unity in liquid.

Modelling of turbulent heat flux $\left(-\rho\overline{u_i' T'}\right)$. Following the same analogy as the Reynolds stress, the turbulent heat flux (Reynolds heat flux) can be written as:

$$-\overline{u_i' T'} = \alpha_t \frac{\partial \overline{T}}{\partial x_i} \tag{6}$$

where, α_t is the eddy thermal diffusivity. From the analogy of laminar flow, α_t can be expressed as:

$$\alpha_t = \frac{\mu_t}{\rho \sigma_t} \tag{7}$$

where σ_t is turbulent Prandtl number. It has been proposed that σ_t varies from 0.8 to 0.9.In the present work, $\sigma_t = 0.9$.

Modelling of turbulent mass flux $\left(-\rho\overline{u_i' C'}\right)$. Following the same analogy as the Reynolds stress, the turbulent mass flux (Reynolds mass flux) can be written as:

$$-\overline{u_i' C'} = \alpha_c \frac{\partial \overline{C}}{\partial x_i} \tag{8}$$

where, α_c is the eddy mass diffusivity. From the analogy of laminar flow, α_c can be expressed as:

$$\alpha_c = \frac{\mu_t}{\rho \sigma_c} \tag{9}$$

where, σ_c is turbulent Schmidt number. It has been proposed that σ_c varies from 0.8 to 0.9.In the present work, $\sigma_c = 0.9$.

Modelling evaporation

A kinetic theory-based approach is adopted for modelling evaporation from the surface of the molten pool. The liquid surface layer formed by laser heating penetrates into the

solid at a rate determined by the quantity of vapour expelled. As the temperature of the liquid increases, the cohesive force in the liquid molecules decreases. As a result, the latent heat of vaporization decreases with the temperature until the critical temperature is reached. The latent heat of vaporization can be given as:

$$L_v = L_0\left[1 - \left(\frac{T_S}{T_C}\right)^2\right] \tag{10}$$

where L_0 is the latent heat of vaporization at absolute zero and T_S, T_C are the surface temperature and critical temperature, respectively. The evaporating surface velocity can be obtained from the surface velocity (Yilbas, 1997) as:

$$V_S = \left(\frac{k_B T}{2\pi m}\right)^{1/2} \exp\left(-\frac{L_v}{k_B T}\right) \tag{11}$$

where m and k_B are the mass per atom and Boltzmann constant, respectively.

In the present model only heat loss due to vaporization is considered, however, material reduction is not considered. The vaporization flux can be obtained from the evaporating surface velocity as:

$$J = \rho_v V_S = \frac{P_S V_S}{RT} \tag{12}$$

where, ρ_v, P_S are the density of the metal vapour and partial pressure, respectively.

The net heat flux due to evaporation is given by JL_v. In the calculations this amount of heat loss from the top surface is added to heat loss due to other modes of heat transfer, i.e. convective heat loss, radiative heat loss. The vapour pressure is a function of temperature and the function depends on the type of material.

Boundary conditions

The boundary conditions for the thermal, solutal and flow variables with reference to the work piece can be stated as follows:

Top surface

The laser power intensity distribution is assumed to be Gaussian across the heated spot, as shown in Figure 2. Considering convective, radiative and evaporative loss, the heat flux at the top surface can be given as:

$$-K\left.\frac{\partial \bar{T}}{\partial y}\right|_{\text{top}} = -\frac{\eta Q}{\pi r_q^2}\exp\left[-\frac{f\left(x^2+z^2\right)}{r_q^2}\right] + h\left(\bar{T} - T_\infty\right) + \varepsilon_r \sigma_{rad}\left(\bar{T}^4 - T_\infty^4\right) + JL_v \tag{13}$$

where, Q is the total arc power, r_q corresponds to the distance from the origin to the location where the power is reduced to 5 per cent of its maximum value, η is the power efficiency, the sign of the heat flux corresponds to the heat flux is in negative y direction, ε_r is the emissivity of the top surface and σ_{rad} is the Stefan–Boltzmann constant.

The top surface velocity boundary condition is given as:

$$\overline{v} = V_S \tag{14}$$

From the free surface shear balance between viscous force and surface tension:

$$\mu \frac{\partial \overline{u}}{\partial y} = \frac{\partial \sigma_{sur}}{\partial T}\frac{\partial \overline{T}}{\partial x} + \frac{\partial \sigma_{sur}}{\partial C}\frac{\partial \overline{C}}{\partial x} \tag{15a}$$

$$\mu \frac{\partial \overline{w}}{\partial y} = \frac{\partial \sigma_{sur}}{\partial T}\frac{\partial \overline{T}}{\partial z} + \frac{\partial \sigma_{sur}}{\partial C}\frac{\partial \overline{C}}{\partial z} \tag{15b}$$

where, $\partial \sigma_{sur}/\partial T$ is the surface tension coefficient of temperature and $\partial \sigma_{sur}/\partial C$ is the surface tension coefficient of concentration. Regarding the transport of k and ϵ, the top surface is assumed to act like an open channel flow (Aboutalebi *et al.*, 1995):

$$\frac{\partial k}{\partial y} = 0, \quad \frac{\partial \varepsilon}{\partial y} = 0 \tag{16}$$

Since the mass flux of the added species at the top surface is assumed to be in a molten state, it can be represented using Fick's first law of diffusion as

$$-\rho D \frac{\partial \bar{C}}{\partial y} = -\dot{m} \tag{17}$$

where, $\dot{m}$ is the mass flux of the alloying element in the negative y direction and D is the mass diffusion coefficient of the alloying element in the substrate material. The mass flux is assumed uniform and is calculated from the powder feed-rate (m_f) as

$$\dot{m} = \frac{m_f}{\pi r_q^2} \tag{18}$$

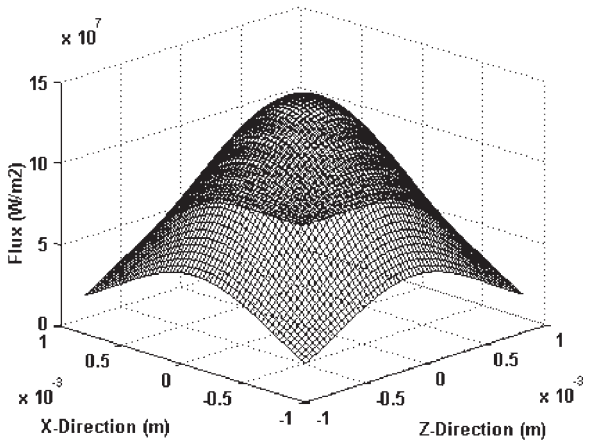

Figure 2.
Laser power intensity distribution

Side faces
The four side faces are subjected to convective heat transfer boundary condition:

$$-K\frac{\partial \overline{T}}{\partial n} = h(\overline{T}_{wall} - T_{\alpha}) \tag{19}$$

where, n is the direction of outward normal to the surface concerned and h is the convective heat transfer coefficient.

Bottom faces
The face being insulated, the temperature boundary condition is:

$$\frac{\partial \overline{T}}{\partial y} = 0 \tag{20}$$

Solid–liquid interface
Regarding interface conditions, it is apparent that the solid/liquid interface in this problem acts as a wall, and the same needs to be treated appropriately. However, according to the enthalpy-porosity formulation, one does not need to track the interface separately and impose velocity or temperature boundary conditions on the same, since the interface comes out as a natural outcome of the solution procedure itself. However, the evolving interface locations are important inputs for k and ε equations, since the values of k and ε are to be specified for near wall points with the help of suitable wall functions, which lead to satisfaction of the following conditions at the solid/liquid interface:

$$k = 0 \tag{21a}$$

$$\frac{\partial \varepsilon}{\partial n} = 0 \tag{21b}$$

It can be noted here that the alloying element added to the pool subsequently mixes with the molten base metal by convection and diffusion. However, at the solidification interface, only a part of solute $k_p\bar{C}$ goes into the solid phase, where k_p is the partition coefficient. Thus, the solute flux balance at the solidification front is given by (Flemings, 1974):

$$-D\frac{\partial \bar{C}}{\partial n} = v_n\bar{C}(1 - k_p) \tag{22a}$$

where n is the direction of outward normal, and v_n is the interface velocity in that direction. Similarly, the boundary condition at the fusion front can be written as (Flemings, 1974):

$$-D\frac{\partial \bar{C}}{\partial n} = v_n\bar{C} \tag{22b}$$

Entropy generation analysis

The entropy generation is estimated following the solution of entropy transport equation along with entropy boundary conditions.

Second law as a transport equation

The second law for an equivalent single-phase can be represented in a form similar to Equation (1), but it includes an inequality, rather than equality, because entropy is typically produced, rather than only conserved.

$$\dot{P}_s \equiv \frac{\partial S}{\partial t} + \nabla \cdot \Psi \geq 0 \tag{23}$$

where $\dot{P}_s, S$ and Ψ are the entropy production rate, entropy and the entropy flux, respectively. Expressing the entropy flux in terms of advective and diffusive components, Equation (23) becomes:

$$\frac{D(\rho s)}{Dt} = \nabla \cdot \left(\frac{K \nabla T}{T}\right) + \nabla \cdot \left(\sum_i \frac{g_i \dot{J}_i}{T}\right) + \dot{P}_s \tag{24}$$

where s, g_i and $\dot{J}_i$ are specific entropy, chemical potential and species flux of constituent i.

Local rate of entropy production

Invoking the Gibbs equation and the entropy transport equation (Naterer and Roach, 1998), the general expression for the rate of local entropy generation in a flow field with both heat and mass transfer can be written as:

$$\dot{P}_s = \frac{K}{T^2}(\nabla T)^2 + \frac{\mu}{T}\Phi - \frac{1}{T}\sum_i \dot{J}_i \cdot \nabla g_i + \frac{1}{T^2}\sum_i g_i \dot{J}_i \cdot \nabla T \tag{25}$$

where, Φ represents the viscous dissipation for a convective flow. For a three-dimensional situation Φ is given as:

$$\begin{aligned}\Phi = 2\left[\left(\frac{\partial u}{\partial x}\right)^2 + \left(\frac{\partial v}{\partial y}\right)^2 + \left(\frac{\partial w}{\partial z}\right)^2\right] + \left[\frac{\partial v}{\partial x} + \frac{\partial u}{\partial y}\right]^2 + \left[\frac{\partial w}{\partial y} + \frac{\partial v}{\partial z}\right]^2 \\ + \left[\frac{\partial u}{\partial z} + \frac{\partial w}{\partial x}\right]^2 - \frac{2}{3}\left[\frac{\partial u}{\partial x} + \frac{\partial v}{\partial y} + \frac{\partial w}{\partial z}\right]^2\end{aligned} \tag{26}$$

From Fick's law of mass diffusion, the species flux of i-th species can be given by $-D_i \nabla C_i$ where, D_i is the mass diffusion coefficient of the i-th species. The chemical potential gradient can be rewritten as $\nabla g_i \approx \nabla C_i$.

Total entropy generation and entropy generation number
The total entropy generation is calculated as follows:

$$P_s = \iiint_V \rho s dV \tag{27}$$

The first law efficiency of the process may be written as:

$$\eta_I = \frac{\text{Actual energy stored in the system}}{\text{Energy supplied the system by laser beam}} = \frac{\iiint_V \rho(cT + \Delta H)\, dV}{\eta Q\, \delta t} \tag{28}$$

where, η is the efficiency of laser heating, Q represents the total laser power and δt is the laser heating time. From the definition, the first law efficiency can be viewed as a ratio of two energies and it reflects the energy losses as a low-grade heat.

For description of the second law efficiency, the entropy generation number (Bejan, 1987) needs to be introduced.

$$N_s = \frac{\text{Total availability destroyed during the process}}{\text{Total availability that enters the system during the process}} = \frac{T_0 P_s}{\eta Q} \tag{29}$$

where T_0 is the initial temperature of the substrate material.

Following the above description of the entropy generation number, the second law efficiency may be expressed as:

$$\eta_{II} = 1 - N_s \tag{30}$$

Numerical implementation

Discretization of conservation equations
The governing equations are discretized using the control volume method, where a whole rectangular computational domain is divided into small rectangular control volumes. A scalar grid point is located at the centre of each control volume, storing the values for scalar variables such as pressure, enthalpy and entropy. In order to ensure the stability of numerical calculation, velocity components are arranged on different grid points, staggered with respect to scalar grid points. Discretized equations for a variable are formulated by integrating the corresponding governing equation over the three-dimensional control volumes. The final discretized equation takes the following form (Patankar, 1980):

$$a_P \phi_P = \sum_{nb} (a_{nb} \phi_{nb}) + a_P^0 \phi_P^0 + \varsigma_U \Delta V \tag{31}$$

where, subscript P represents a given grid point, while subscript nb represents the neighbours of the given grid point P, ϕ is a general variable such as velocity or enthalpy, a is the coefficient calculated based on the power law scheme, ΔV is the volume of the control volume, a_P^0 and ϕ_P^0 are the coefficient and value of the general variable at the previous time step, respectively. The coefficient a_P is defined as:

$$a_P = \sum_{nb} a_{nb} + a_P^0 - \varsigma_P \Delta V \tag{32}$$

The terms ς_U and ς_P are used in the source term linearization as:

$$\varsigma = \varsigma_U + \varsigma_P \phi_P \tag{33}$$

The coupled conservation equations are then solved iteratively on a line-by-line basis using a tri-diagonal matrix algorithm following a pressure-based finite volume method according to the SIMPLER algorithm (Patankar, 1980). The latent heat content of each control volume is updated using the temperature field obtained from energy equation, as outlined in Brent *et al.* (1988).

Discretization of second law of thermodynamics
Integrating Equation (23) over a control volume and time step, one can write

$$\int_V \int_t^{t+\Delta t} \frac{\partial S}{\partial t} dt\, dV + \int_t^{t+\Delta t} \int_V (\nabla \cdot \Psi) dV\, dt \geq 0 \tag{34}$$

Performing the integration in Equation (34) for a discrete volume ΔV and following an implicit formulation over the time step $\Delta t = t^{n+1} - t^n$, one obtains:

$$\dot{P}_s \equiv \left(\frac{S_i^{n+1} - S_i^n}{\Delta t} \right) \Delta V + \left[\sum_{nb} \Psi_{nb} \right]^{n+1} \geq 0 \tag{35}$$

The Gibbs equation is invoked here to represent the transient entropy derivative in Equation (35) in terms of variables obtained from solution of the conservation equations, such as temperature and liquid fraction.

$$\frac{S_i^{n+1} - S_i^n}{\Delta t} = \frac{\rho c}{T_i^n} \left(\frac{T_i^{n+1} - T_i^n}{\Delta t} \right) + \rho \Delta S_f \left(\frac{f_{l,i}^{n+1} - f_{l,i}^n}{\Delta t} \right) \tag{36}$$

where, $\Delta S_f = s_l - s_s$ refers to the entropy of fusion (approximately equal to the heat of fusion divided by the phase change temperature).

Discretization of entropy equation of state
An entropy equation of state is also required for the implementation of the second law. Considering entropy as a function of temperature and concentration a piecewise logarithmic equation of state following Gibbs equation for an incompressible substance is assumed.

$$s(T, C) = s_{r,k} + C_{r,k} \ln \left(\frac{T}{T_{r,k}} \right) \tag{37}$$

where, the subscripts r and k denote reference and phase respectively. The following reference values are used depending on the computed value of the liquid fraction.

$$\left.\begin{aligned} s_{r,s} &= 0 \\ C_{r,s} &= C_s \\ T_{r,s} &= T_e \end{aligned}\right\} \quad \text{for } f_l = 0$$

$$\left.\begin{aligned} s_{r,m} &= C_s \ln(T_s/T_e) \\ C_{r,m} &= \left(\frac{C_s T_l - C_l T_s}{T_l - T_s}\right) + \frac{C_l - C_s + \Delta S_f}{\ln(T_l/T_s)} \\ T_{r,m} &= T_s \end{aligned}\right\} \quad \text{for } 0 < f_l < 1 \tag{38}$$

$$\left.\begin{aligned} s_{r,l} &= \left(\frac{C_s T_l - C_l T_s}{T_l - T_s}\right) \ln\left(\frac{T_l}{T_s}\right) + C_s \ln\left(\frac{T_s}{T_e}\right) + C_l - C_s + \Delta S_f \\ C_{r,l} &= C_l \\ T_{r,l} &= T_l \end{aligned}\right\} \quad \text{for } f_l = 1$$

where, the subscripts s, l, m and e denote the solid, liquid, mushy (two-phase) region and eutectic composition.

Entropy boundary condition

Introducing the entropy equation of state closes the entropy equations for interior control volumes. However, closure is still required for the boundary control volumes. The inflow and outflow of entropy are required to be computed for closure of the second law in the boundary control volumes.

The boundary entropy production rate is directly computed from Equation (25) using the spatial derivatives of temperature, velocity and concentration. The interfacial entropy balance can be given as:

$$P_{s,i} = \frac{\rho_s}{\rho_l}\left(\Delta S_f - \frac{L}{T}\right) + \frac{K_l}{\rho_l V_l}\left.\frac{dT}{dn}\right|_l \left(\frac{1}{T_l} - \frac{1}{T_s}\right) \geq 0 \tag{39}$$

Grid spacing and time step

In order to capture the top surface velocity originating from surface tension gradients, the choice of grid-size should be judicious. This also ensures indirectly that the calculations for velocity gradients are accurate enough, so that the turbulent source terms can be properly evaluated. In order to capture sufficient flow details inside the surface tension driven boundary layer at the top surface, at least a few (typically five) grid points are accommodated inside the same. In order to specify the diffusion coefficients near the wall using wall conditions (Chen and Law, 1998), it is necessary to control the grid size in the vicinity. Otherwise, it can be possible that the grid points immediately next to the wall will fall beyond the "near wall" regime. Accordingly, we choose a depth of 4.0×10^{-6} m for the topmost grids. Just below this, the grid depths are taken as 8.0×10^{-6} m, followed by a depth of three grid spacing of 1.2×10^{-5} m. Then 2.4×10^{-5} m, 4.1×10^{-5} m, 4.9×10^{-5} m, 5.3×10^{-5} m and 9.8×10^{-5} m, respectively, in negative y direction. Thereafter a uniform grid depth of 3.75×10^{-4} m is employed for most of the remaining part of the pool. The grid spacing is made coarser in y-direction gradually. Outside the molten pool, a non-uniform coarse grid is chosen. In the x and z direction, an optimized grid size near the wall is found to be

6.45×10^{-5} m, after which the grid size is increased gradually to 2.66×10^{-4} m away from the wall. Overall, a $69 \times 35 \times 69$ grid system is used to discretize the working domain (8 mm $\times$ 4 mm $\times$ 8 mm). A comprehensive grid independence study has been carried out for a set of different sized grids as shown in Table II. It is found from the study that the present grid turns out to be a reasonable optimization from the point of view of numerical accuracy and computational economy.

During the conduction dominated initial stage of melting (unto 0.005 s) a larger time step (about 0.001 s) is chosen. However, with the inception of melting, the high temperature gradient in the pool sets up a strong Marangoni convection, leading to convection dominated flow field. It is observed that time step only as small as about 0.0005 s lead towards monotonic convergence during this period. Typically after about 0.025 s, the molten pool reaches a state, when changes in dependent variables between the consecutive time steps are relatively small. At this stage, slightly higher time steps (typically about 0.001 s) can safely be used to save computational time. After 0.5 s, the pool becomes sufficiently developed, which allows time steps as high as 0.002 *s* without any oscillation. Finally, the simulation is carried out unto 1.5 s in order to achieve a quasi-steady state. During this period, the maximum relative variations in the values of dependent variables between two consecutive time steps are found to be less than 10^{-5} per cent.

Convergence criteria

Within a particular time step, convergence for all the independent variable $(\bar{u}, \bar{v}, \bar{w}, \bar{C}, k, \varepsilon)$ values are checked after each iteration. It is taken that convergence has been achieved if the following tolerance is satisfied at each grid point:

$$\left| \frac{\phi - \phi_{old}}{\phi_{\max}} \right| \leq 10^{-4} \tag{40}$$

where ϕ is the value of the general variable at a particular grid point at current iteration level, ϕ_{old} is the value of the general variable at the same grid point at the previous iteration level and $\phi_{\max}$ is the maximum absolute value of the same over the entire domain.

Results and discussion

On general transport phenomena

The mathematical model is applied to the case of LSA of aluminium on nickel substrate. The physical property values are taken from Mohanraj *et al.* (2002). The

Grid size	% error in maximum velocity	% error in maximum temperature	% error in maximum concentration
$49 \times 25 \times 49$	1.06	1.02	1.09
$59 \times 30 \times 59$	0.99	0.97	1.01
$79 \times 40 \times 79$	0.97	0.98	0.95

Table II.
Grid sensitivity study

Note: The percentage error is calculated using $\{\phi - \phi_z\}/\phi$, where ϕ_z is based on $69 \times 35 \times 69$ grid system

velocity, temperature and concentration contours obtained from the numerical simulation are shown in Figures 3-5. The results correspond to a typical value of process parameters ($u_{scan} = 0.012$ m/s, $Q = 2.4$ kW, $\eta = 0.15$, $m_f = 0.02$ gm/s).

A radially outward velocity vectors from the point of laser impact are observed on the top surface of the substrate. This type of outward fluid motion is a regular consequence of the negative surface tension coefficient of temperature of the substrate

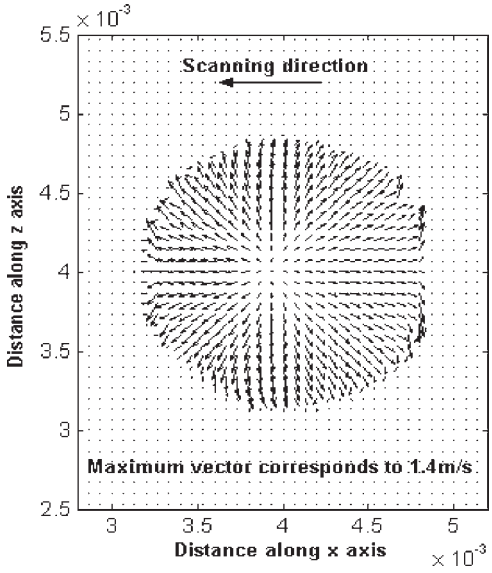

Figure 3.
Top view of velocity (m/s) vector plots

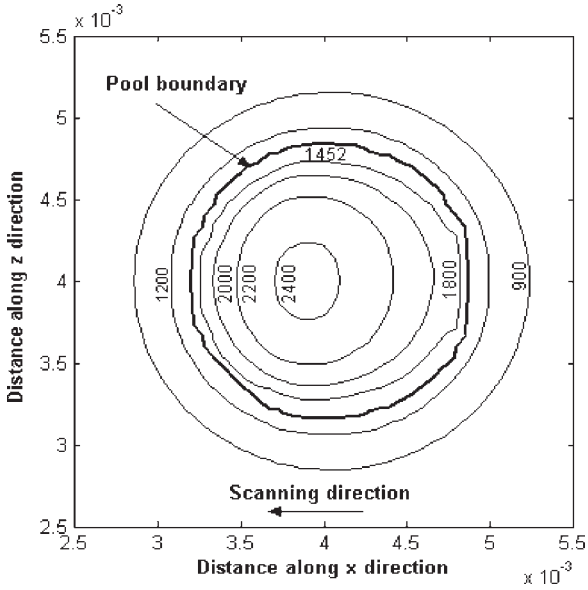

Figure 4.
Top view of temperature (°C) field

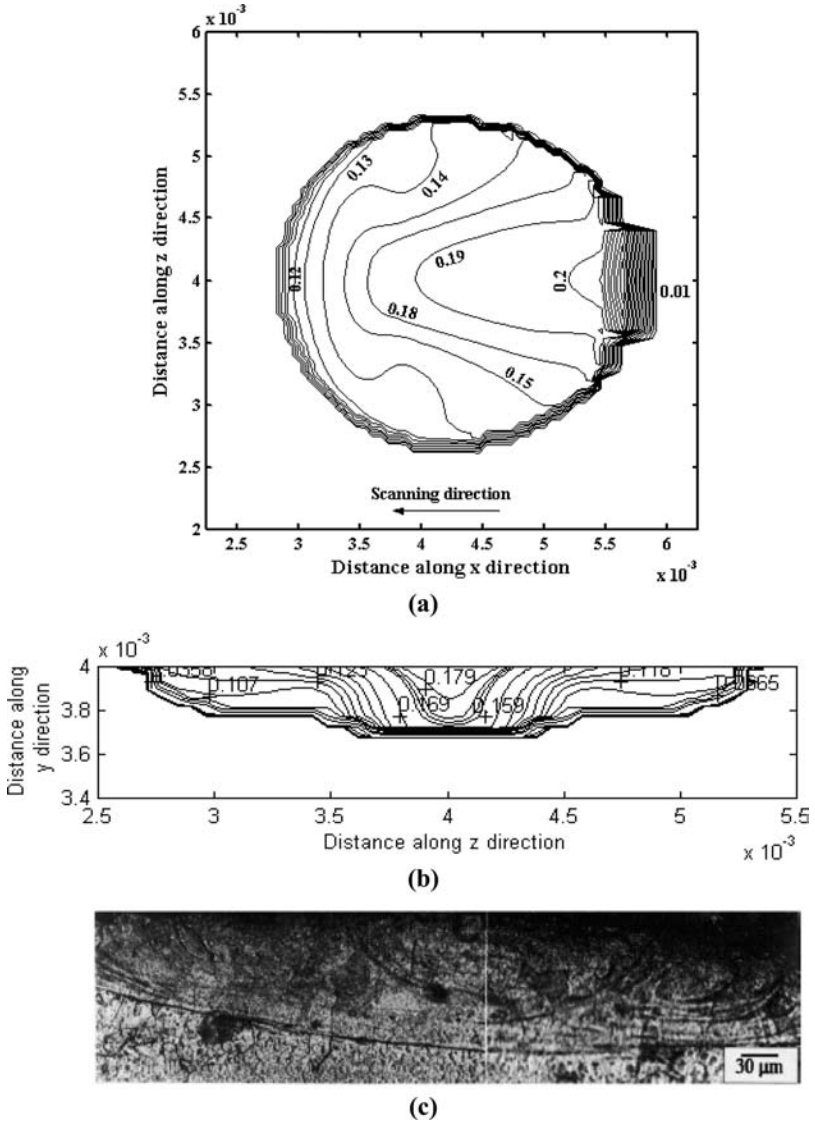

Figure 5.
Solute concentration field: (a) top view, (b) at cross-sectional mid-plane, (c) micrography of an experimental section

material. It should be mentioned here that the liquid flow is mainly driven by surface tension force and to a much less extent by the buoyancy force. This fact can be supplemented by a dimensional analysis. The ratio of buoyancy force to viscous force is determined by Grashof number, which is given as:

$$Gr = Gr_T + Gr_C = \frac{g\beta_T \Delta T l_{ref,t}^3 \rho^2}{\mu^2} + \frac{g\beta_C \Delta C l_{ref,c}^3 \rho^2}{\mu^2} \tag{41}$$

where Gr_T and Gr_C are the thermal and solutal Grashof numbers, ΔT and ΔC are the temperature and concentration differences between the peak values and the

corresponding eutectic values and $l_{ref,t}$ and $l_{ref,c}$ are the characteristic lengths which are chosen to be the thermal and concentration boundary layer thicknesses, respectively. The surface tension Reynolds number or the Marangoni number (Ma) is given by the ratio of surface tension gradient force to viscous force as:

$$Ma = \frac{\rho l_{ref,v} \Delta T |\partial \sigma_{sur} / \partial T|}{\mu^2} + \frac{\rho l_{ref,c} \Delta C |\partial \sigma_{sur} / \partial C|}{\mu^2} \tag{42}$$

where $l_{ref,v}$ is the characteristic length given by the viscous boundary layer thickness.

Using the physical properties from Mohanraj *et al.* (2002), the corresponding values of Grashof and Marangoni numbers are estimated as 0.8195 and 10950.5. The ratio of surface tension force to buoyant force is expressed as:

$$R_{s/b} = \frac{Ma}{Gr} = \frac{10950.5}{0.8195} = 1.336 \times 10^4 \tag{43}$$

Hence, it can be concluded that the liquid flow is mainly induced by the Marangoni convection and to a lesser extent by the buoyancy force.

The temperature contours as observed from Figure 4, are almost concentric circles. This type of geometry is a consequence of the anisotropic nature of an enhanced diffusion process in case of turbulent molten pool. In the present case, the net thermal energy available to the pool is predominantly transported along the longitudinal and sidewise directions by the Marangoni advection along with molecular as well as eddy thermal diffusion process. The downward advection of heat is small compared to longitudinal and span wise advection because of much smaller magnitude of downward velocity component, as compared to magnitudes of longitudinal and span wise components. In case of turbulent transport, due to an enhanced mixing process on account of an efficient energy cascading mechanism taking place between participating eddies, the mean advection strength goes down, which results in a decrease in longitudinal and sidewise advection strength. On the other hand, an enhanced effective diffusion process due to interactions between fluctuating velocity components of eddies in a turbulent pool tries to increase the length and width of the pool by propagating the influence of thermal disturbance across a relatively larger distance. The resultant pool geometry is, therefore, a consequence of the above two counteracting effects active in tandem.

The distribution of aluminium concentration in the molten pool is shown in Figure 5. It is evident from the above figure that the concentration of solute is higher near the solidification front and gradually decreases toward the melting front. At the melting front, dilution of species takes place due to fresh addition of molten base metal. On the contrary, since solubility of the solute in the solid phase is less than that in the liquid phase for the present case, there will be preferential solute rejection from the solidified material back into the molten pool at the solidification front. The rejected solute is transported back into the centre of the pool as a consequence of the combined advection-diffusion field.

It is apprehended that the simulation results of the transport processes occurring inside the laser molten pool can provide better insight of the nature of microstructure that would be expected. As a visual appreciation a micrography of an experimental section (Mohanraj *et al.*, 2002) is shown in Figure 5(c) along with the numerically

obtained solute concentration distribution at the cross-sectional mid-plane. The comparison shows an excellent experimental agreement of the present model and also demonstrates the capability of the model to predict the nature of the evolved microstructure.

On entropy generation

The total entropy generation consists of entropy generation due to heat transfer, mass transfer, fluid friction and combined heat and mass transfer. However, entropy generation due to heat transfer is found to contribute about 99 per cent of the total

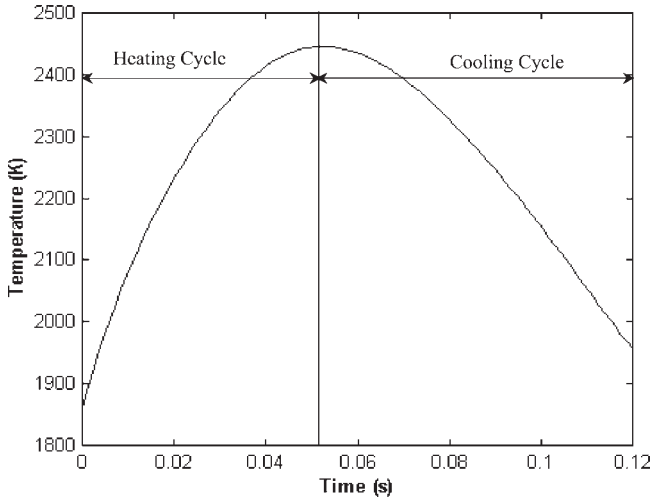

Figure 6.
Variation of temperature with time in a longitudinal section along the direction of laser scanning

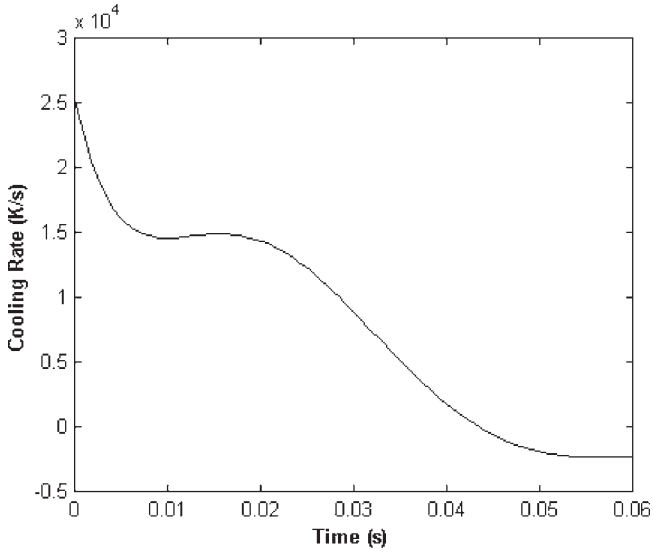

Figure 7.
Variation of cooling rate with time in a longitudinal section along the direction of laser scanning

entropy generation. Hence, it is important to observe the temperature response of the substrate material due to laser heating on the context of entropy generation.

Figure 6 shows the temporal variation of the top surface temperature in a longitudinal section along the direction of laser scanning. The curve shows a steeper gradient near the melting front than near the solidification front. Also, beneath the tip

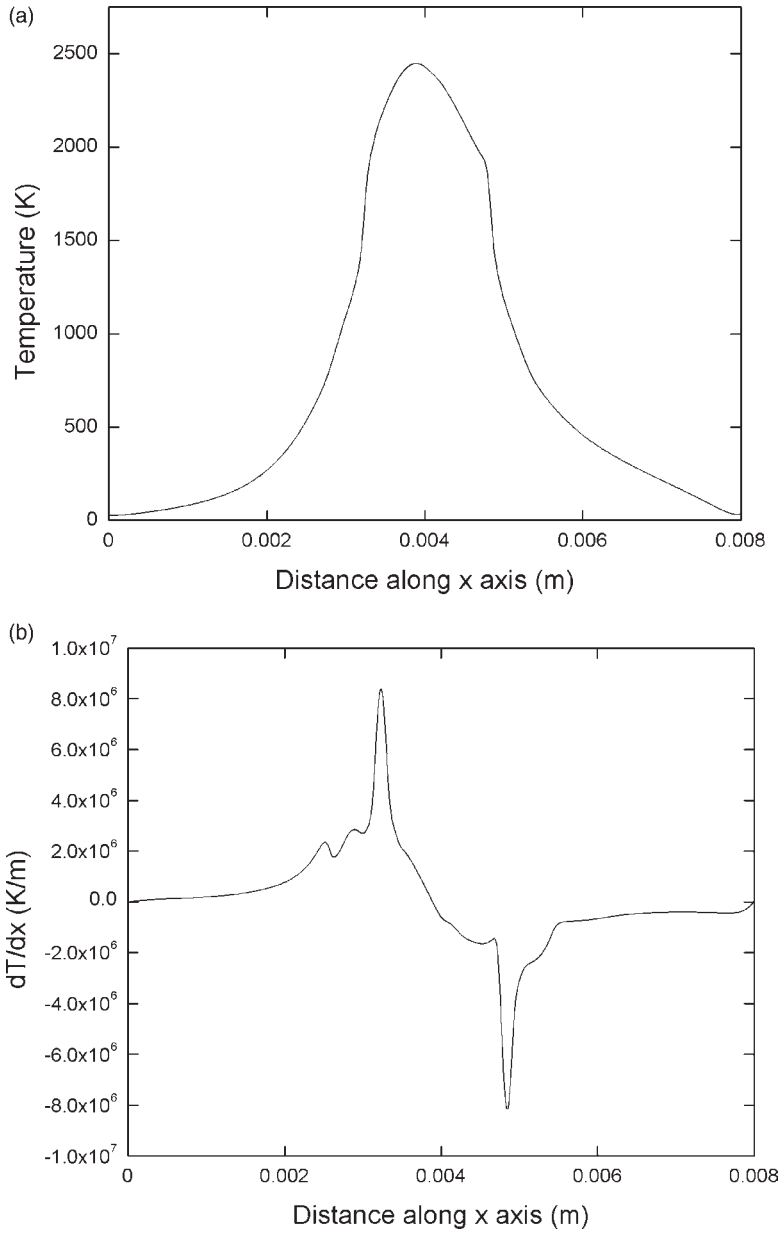

Figure 8.
(a) Temperature variation along x-axis on the top surface, (b) variation of dT/dx along x-axis on the top surface

of the laser, the temperature reaches its peak. The nature of the curve is consistent with the Gaussian heat input (refer to Figure 2). Figure 7 shows the variation of cooling rate with time. The cooling rate is maximum at the early stage of heating and reduces thereafter. This type of curve is an important basis for the prediction of the microstructure of the resolidified pool. Figures 8(a) and 9(a) shows the temperature profiles along *x*-axis and *y*-axis on the top surface and at the longitudinal mid-plane,

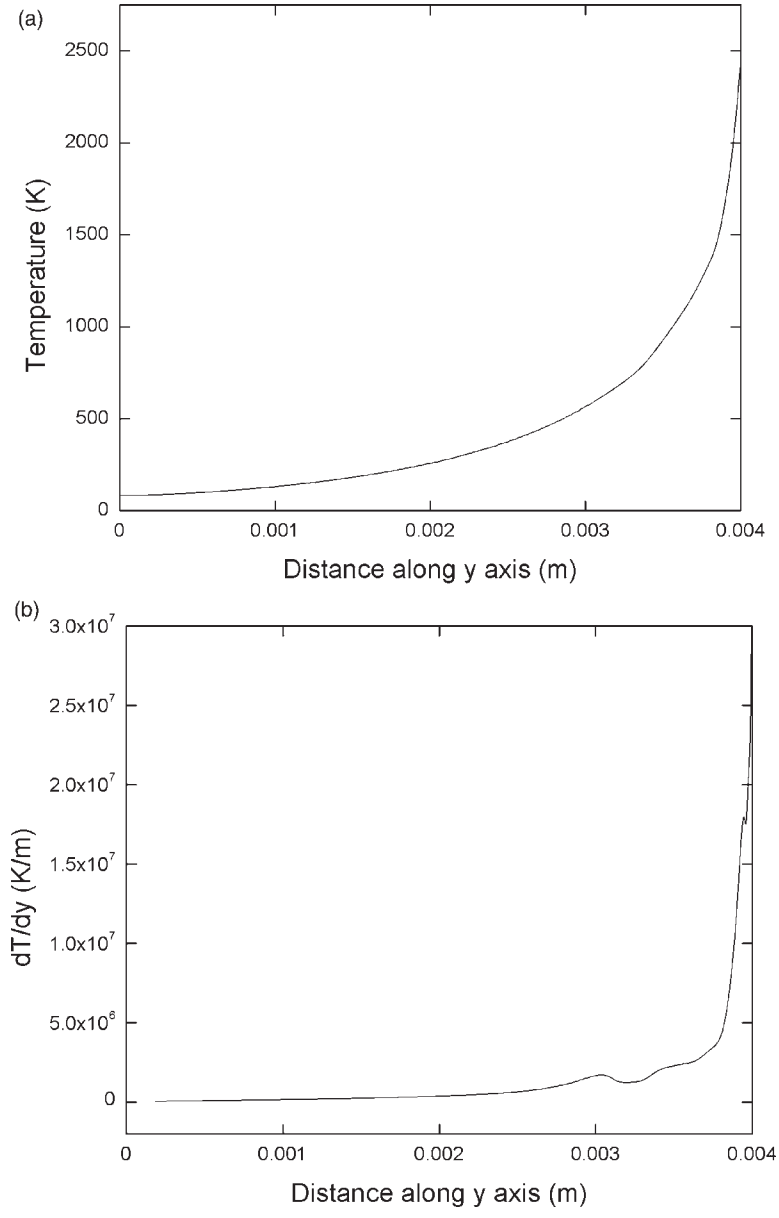

Figure 9.
(a) Temperature variation along *y*-axis at the longitudinal mid-plane, (b) variation of *dT*/*dy* along *y*-axis at the longitudinal mid-plane

respectively. The temperature attains a maximum value rapidly near the irradiated spot centre. In the region close to the irradiated spot centre the substrate gains considerable energy from the incident laser beam. This energy is then transported throughout the material surface by conduction and convection. The variation of temperature gradients as shown in Figures 8(b) and 9(b) has got strong influence on the

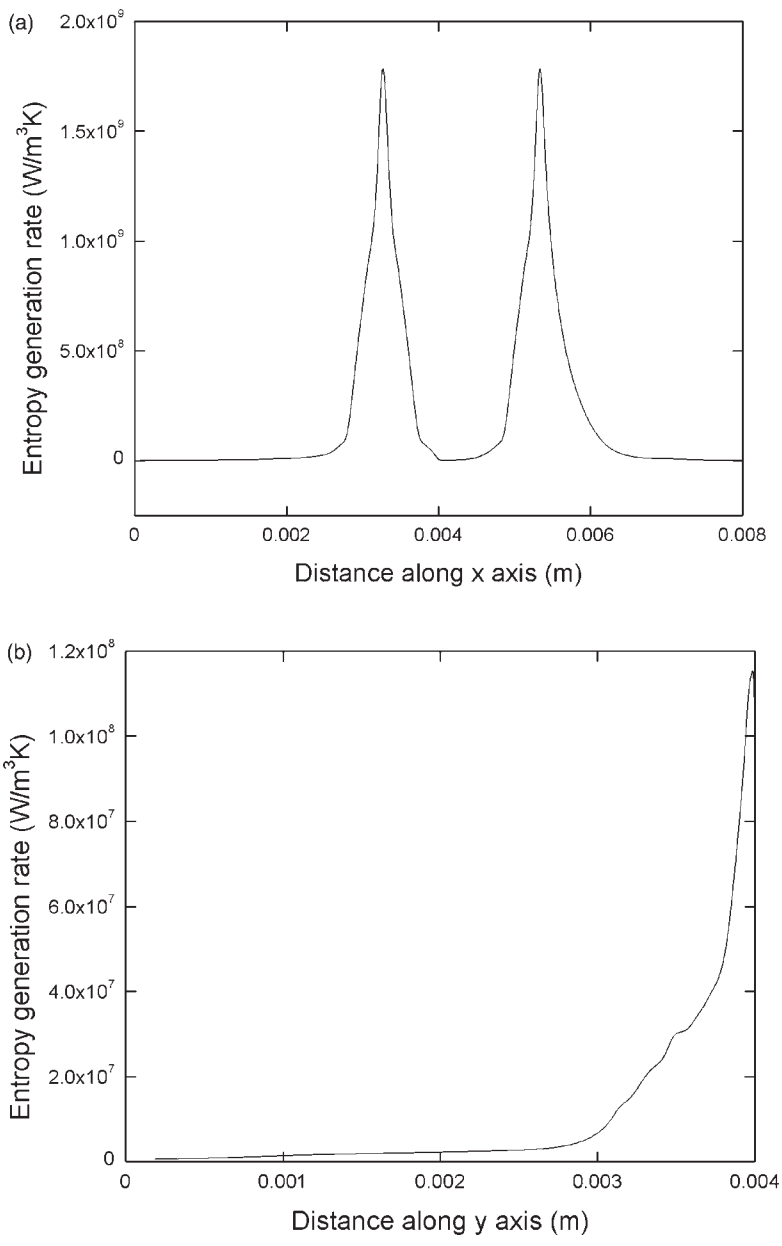

Figure 10.
(a) Variation of entropy generation rate along *x*-axis on the top surface, (b) variation of entropy generation rate along *y*-axis at the longitudinal mid-plane

entropy production rate. The local entropy production rate is directly proportional to the square of the temperature gradient. In Figure 8(b) the temperature gradient is found to be symmetrical about the central cross-sectional plane, which ensures that the entropy production rate will also be symmetrical about the same plane as shown in Figure 10(a). Figure 9(b) shows that the maximum variation of temperature gradient is limited to a thin layer from the top surface of the substrate material. This is due to the fact that the main mode of heat transfer in the vertical direction is conduction. As expected the entropy generation rate curve along *y*-axis (Figure 10(b)) shows the same nature qualitatively with the temperature gradient. Further, spikes in the temperature gradient at the edges of the molten pool are observed which can be attributed by the fact that the main mode of heat transfer in the molten pool is convection whereas outside the molten pool it is conduction. Hence there is a drastic change of the temperature gradient at the edge of the molten pool and accordingly the spikes are observed.

On efficiency analysis

The variations of first law and second law efficiency with effective heat input, scanning speed and powder feed rate are shown in Figures 14-16. The maximum first law efficiency is found to be around 0.7, which is considerably high, whereas the maximum second law efficiency is around 0.3. This indicates that the useful work done on the substrate material is considerably less. The nature of variation of efficiency can be explained with the help of the nature of variation of temperature as shown in Figures 11-13. In Figure 11 shown the variation of maximum temperature with effective heat input. The temperature is expected to increase with the heat input, as the internal energy gain of the workpiece increases with the laser power input. As a consequence of the substantial increase in the internal energy gain of the substrate, the first law efficiency increases as evident from Figure 14. The total availability that destroyed during the process as well as the total availability that enters the system increase with the increase in maximum temperature or effective heat input. However, the rate of

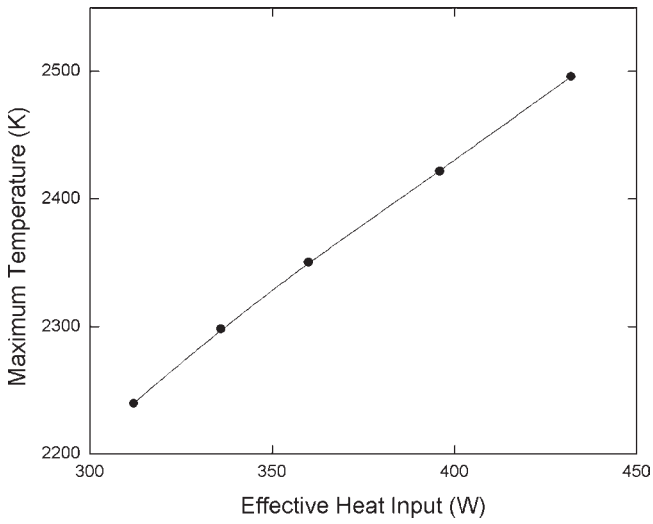

Figure 11.
Variation of maximum temperature with effective heat input

increase of the total availability entering the system is more than the rate of increase of the total availability destroyed during the process. As a result, the entropy generation number decreases and consequently second law efficiency increases with the effective heat input, as shown in Figure 14. The maximum temperature rise is found to decrease with laser scanning speed which is the direct consequence of the reduction in the internal energy gain due to the smaller laser-material interaction time (refer to Figure 12). Due to the reduction of the laser heating time with an increase in the scanning speed, the energy supplied by the laser to the system decreases and the rate of reduction of this energy is more than the rate of reduction of the internal energy gain of

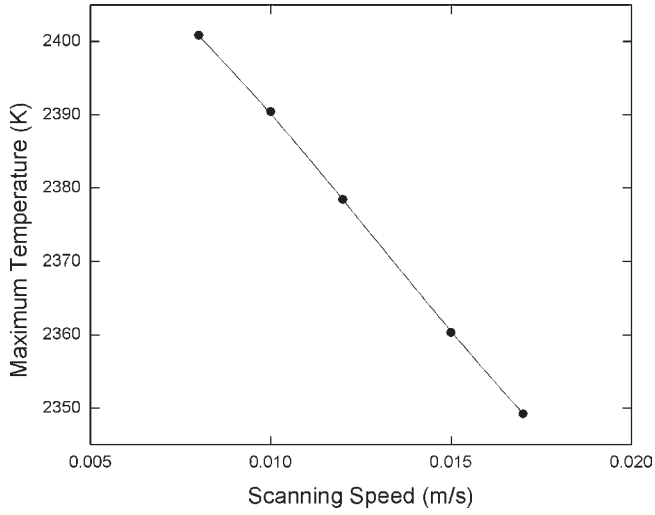

Figure 12.
Variation of maximum temperature with scanning speed

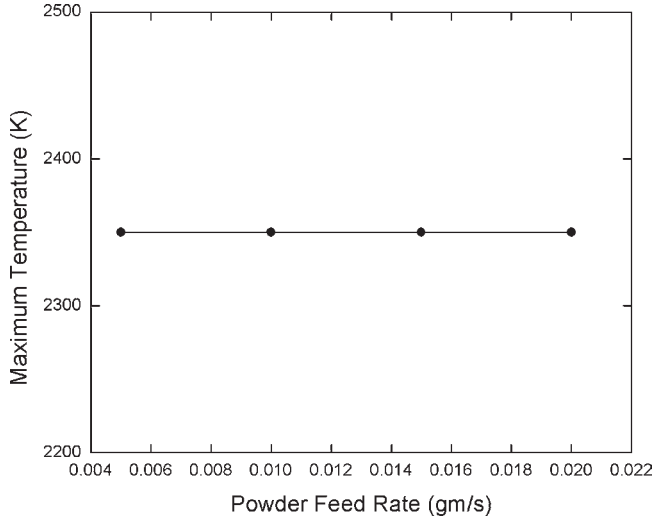

Figure 13.
Variation of maximum temperature with powder feed rate

the substrate. Consequently, the first law efficiency is found to increase with the scanning speed for the same laser power, which can be seen from Figure 15. Also the second law efficiency decreases with the scanning speed (Figure 15), which is self explanatory. From Figure 13 it is evident that the maximum temperature rise in the substrate material is independent of the powder feed rate as the first and second law efficiencies are also independent of the powder feed rate (See Figure 16) which indicates that the mass transfer has got very little impact on the overall entropy generation.

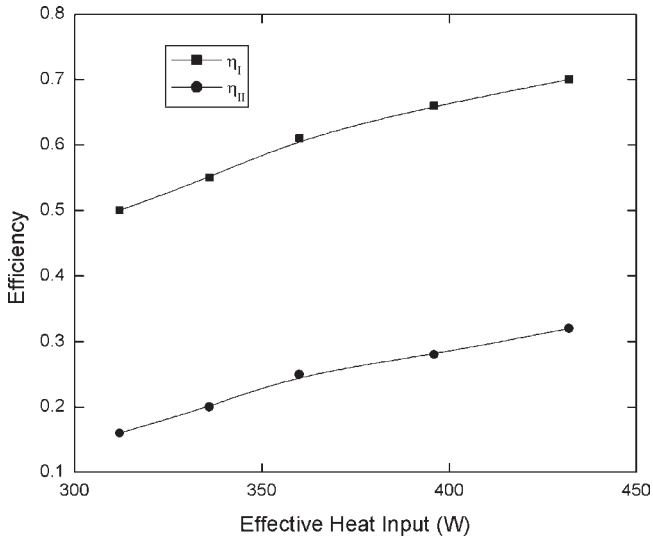

Figure 14.
Variation of first and second law efficiency with effective heat input

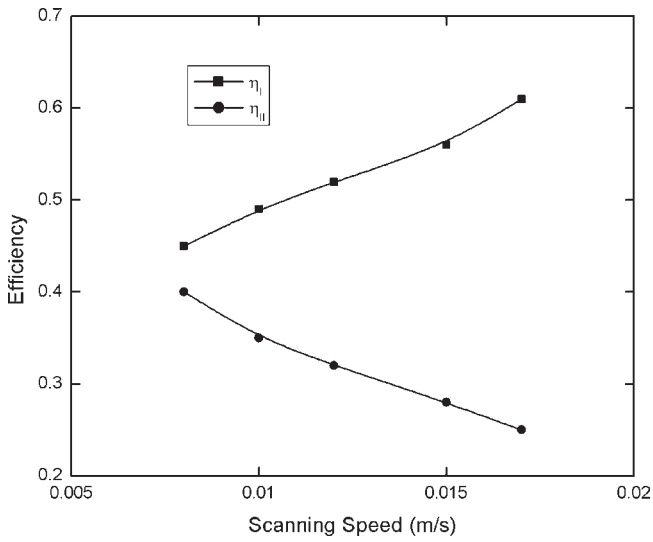

Figure 15.
Variation of first and second law efficiency with scanning speed

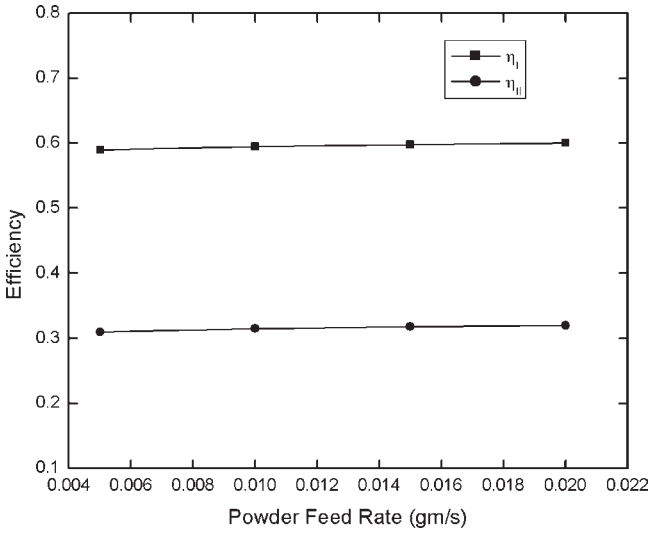

Figure 16.
Variation of first and second law efficiency with powder feed rate

Conclusions

A three-dimensional transient turbulent model is developed and a finite-volume-based entropy generation analysis is carried out to predict the first and second law efficiencies for a typical high power LSA process. It is anticipated that the turbulence modelling will provide better understanding of the molten pool transport phenomena. The Marangoni convection is found to be more dominant than the buoyancy driven convection in molten pool. A general observation is that the enhanced diffusive mixing due to turbulence leads to the substantial homogenization of the velocity, temperature and concentration fields inside the pool, which signifies that the turbulence modelling is necessary for such type of flow simulation. It has also been anticipated that the heat transfer due to the strong temperature gradient is mainly responsible for the irreversible degradation of energy in the form of entropy production and the flow and mass transfer effects are less important for this type of phase change problem. The first and second law efficiencies are found to increase with effective heat input and remain independent of the powder feed rate. With the scanning speed, the first law efficiency increases whereas the second law efficiency decreases. These information will eventually lead to an optimized estimation of laser parameters (such as laser power, scanning speed, etc.), which in turn improves the process control and reduces the cost substantially.

References

Aboutalebi, M.R., Hassan, M. and Guthrie, R.I.L. (1995), "Numerical study of coupled turbulent flow and solidification for steel slab clusters", *Numerical Heat Transfer*, Vol. 28, pp. 279-99.

Badar, M.A., Zubair, S.M. and Al-Ferayedhi, A.A. (1993), "Second law based thermoeconomic optimisation of a sensible heat thermal energy storage system", *Energy – The International Journal*, Vol. 18, pp. 641-9.

Bejan, A. (1982a), "Second law analysis in heat transfer and thermal design", *Advances in Heat Transfer*, Vol. 15, pp. 1-58, Academic Press, New York, NY.

Bejan, A. (1982b), *Entropy Generation Through Heat and Fluid Flow*, John Wiley and Sons, New York, NY.

Bejan, A. (1987), "The thermodynamic design of heat and mass transfer process and devices", *Heat and Fluid Flow*, Vol. 8, pp. 258-76.

Brent, A.D., Voller, V.R. and Reid, K.J. (1988), "Enthalpy-porosity technique for modelling convection-diffusion phase change: application to the melting of a pure metal", *Numerical Heat Transfer*, Vol. 13, pp. 297-318.

Chen, C.J. and Law, S.Y. (1998), *Fundamentals of Turbulence Modelling*, Taylor & Francis, Philadelphia, PA.

Flemings, M.C. (1974), *Solidification Processing*, McGraw-Hill, New York, NY.

Haddad, O.M., Abu-Qudais, M., Abu-Hijleh, B. and Maqableh, A.M. (2000), "Entropy generation due to laminar forced convection flow past a parabolic cylinder", *International Journal of Numerical Methods for Heat and Fluid Flow*, Vol. 10, pp. 770-9.

Komatsu, T. and Matsunaga, N. (1986), "Defect of $\varepsilon-$k turbulence model and its improvements", *Proceedings of 30th Japan Conference on Hydraulics*, pp. 529-34.

Krane, B.J. (1985), "A second law analysis of a thermal energy storage with Joulean heating of the storage element", ASME paper 85-WA/HT-19.

Krane, B.J. (1987), "A second law analysis of the optimum design and operation of thermal energy storage systems", *International Journal of Heat Mass Transfer*, Vol. 30, pp. 43-57.

Mathiprakasam, B. and Beeson, J. (1984), "Second law analysis of thermal energy storage devices", *Heat transfer-Seattle, AIChE Symposium Series*, pp. 161-8.

Mohanraj, P., Sarkar, S., Chakraborty, S., Phanikumar, G., Dutta, P. and Chattopadhyay, K. (2002), "Modelling of transport phenomena in laser surface alloying with distributed species mass source", *International Journal of Heat and Fluid Flow*, Vol. 23, pp. 298-307.

Naterer, G.F. and Roach, D.C. (1998), "Entropy and numerical stability in phase change problems", AIAA paper 98-2765, *AIAA/ASME 7th Joint Thermophysics and Heat Transfer Conference*, *Albuquerque*, *NM*, *15-18 June*.

Patankar, S.V. (1980), *Numerical Heat Transfer and Fluid Flow*, Hemisphere, Washington DC.

Shuja, S.Z., Yilbas, B.S. and Budair, M.O. (2002), "Investigation into a confined laminar swirling jet and entropy production", *International Journal of Numerical Methods for Heat and Fluid Flow*, Vol. 12, pp. 870-87.

Shuja, S.Z., Yilbas, B.S. and Budair, M.O. (2007), "Entropy generation due to jet impingement on a surface: effect of annular nozzle outer angle", *International Journal of Numerical Methods for Heat and Fluid Flow*, Vol. 17, pp. 677-91.

Yilbas, B.S. (1997), "Laser heating process and experimental validation", *International Journal of Heat Mass Transfer*, Vol. 40, pp. 1131-43.

Yilbas, B.S. (1999), "Three-dimensional laser heating model and entropy generation consideration", *Journal of Energy Resources Technology*, Vol. 121, pp. 217-24.

Corresponding author
Dipankar Chatterjee can be contacted at: rsdchat@yahoo.co.in